PHYSICAL REVIEW B **109**, 104107 (2024)

Polymorphic charge density waves, magnetism, and topologies in $1T$-TaTe$_2$

Wei Wang,[1,*] Kang Zhang,[1,*] Yang Liu,[1] Ao Li,[1] Jing Li,[2] and Chen Si[1,†]
[1]*School of Materials Science and Engineering, Beihang University, Beijing 100191, China*
[2]*Medical Engineering Laboratory of Chinese PLA General Hospital, Beijing 100853, China*

(Received 23 August 2023; revised 26 January 2024; accepted 14 February 2024; published 11 March 2024)

Polymorphism in two-dimensional (2D) materials presents a fertile ground for introducing new functionalities and designing novel architectures. Here, using first-principles calculations, we investigate the polymorphs of monolayer $1T$-TaTe$_2$, including the high-symmetry phase and various charge density wave (CDW) phases (3×1, 4×1, 3×3, $2\sqrt{3} \times 2\sqrt{3}$, $\sqrt{13} \times \sqrt{13}$, 4×4, and $\sqrt{19} \times \sqrt{19}$) with diverse physical properties. The high-symmetry $1T$ phase is predicted to be a quantum anomalous Hall metal with ferromagnetism. However, after undergoing the CDW phase transitions, the ferromagnetism vanishes and the nontrivial topological properties are also altered. Particularly, the 4×4 CDW phase with the second lowest total energy exhibits a novel topological insulating state, while the 3×3 CDW phase, possessing the lowest total energy, behaves as a normal metal. We further propose that charge doping can effectively modulate the relative stability of the CDW phases. Upon introducing slight hole doping, the 4×4 CDW becomes the most energetically stable state followed by the 3×3 CDW phase. These findings show the rich landscape of structures and properties of $1T$-TaTe$_2$, which will strongly stimulate further investigations and lay the foundation for the development of new electronic devices.

DOI: 10.1103/PhysRevB.109.104107

I. INTRODUCTION

Polymorphism, which refers to the phenomenon of a solid material existing in multiple crystal structures, is a fundamental and remarkable principle in materials science and condensed matter physics [1]. Particularly, telluride-based transition metal dichalcogenides (TMDCs) contain not only the traditional trigonal ($1T$), hexagonal ($2H$), and rhombohedral ($3R$) phases, but also the distorted $1T$ polytype (such as $1T'$ and $1T''$) as well as various charge density wave (CDW) phases [2–8]. These diverse crystal structures give rise to markedly contrasting electronic properties, thereby offering a unique avenue for the design of materials with predefined functionalities. MoTe$_2$ serves as a prime example: thanks to its rich polymorphism, numerous exotic quantum states have been discovered, including the quantum spin Hall (QSH) effect in the $1T'$ phase, the Weyl semimetal state in the T_d phase, the direct band gap semiconductor in the $2H$ phase, and so on [9–11].

In contrast to S- and Se-based TMDCs which have received extensive attention in recent years [12–21], Te-based TMDCs are still largely unexplored [22–24]. They usually possess relatively strong interlayer Te-Te coupling, inducing unique physical properties distinguished from S/Se compounds and exhibiting striking thickness-dependent features. $1T$-TaTe$_2$, recognized as a prototypical CDW material, is a representative. Different from the $\sqrt{13} \times \sqrt{13}$ CDW orders in bulk $1T$-TaS$_2$ and $1T$-TaSe$_2$, a distinctive 3×1 CDW order characterized by a double zigzag stripe arises in bulk $1T$-TaTe$_2$ at room temperature, forming the so-called distorted $1T$ structure [25–33]. As temperature further decreases, $1T$-TaTe$_2$ undergoes another CDW transition from the 3×1 phase to the 3×3 phase around 170 K, accompanied with abnormal phenomena in heat capacity, magnetic susceptibility, resistivity, and transport [33,34].

Interestingly, recent experiments have revealed that, after removing the interlayer coupling, monolayer $1T$-TaTe$_2$ exhibits a variety of coexisting CDW phases, completely distinct from the isostructural and isoelectronic monolayer $1T$-TaS$_2$ and $1T$-TaSe$_2$ [35,36]. Through molecular beam epitaxy (MBE) techniques, Hwang *et al.* successfully synthesized the single-layer $1T$-TaTe$_2$ and observed the emergence of the $\sqrt{19} \times \sqrt{19}$ CDW phase after high-temperature annealing [35]. They further found that the angle-resolved photoemission spectroscopy (ARPES) results are dramatically modulated by reducing the annealing temperature, and then speculated that there might be a coexistence of the 3×3 and $\sqrt{13} \times \sqrt{13}$ CDW phases within a conventional low-temperature annealing process [35]. At 77 K, Bernardo *et al.* directly observed the coexistence of the 3×1, 3×3, and $\sqrt{19} \times \sqrt{19}$ CDW phases in monolayer $1T$-TaTe$_2$ [36]. Current reports suggest that the CDW phases are susceptible to the annealing temperature and growth condition, indicating the potential presence of hidden CDW phases in monolayer $1T$-TaTe$_2$. Indeed, recent studies on monolayer $1T$-NbTe$_2$ have revealed that, by controlling the growth and annealing temperatures, two different kinetic paths can be generated, thereby enabling the fabrication and manipulation of various CDW phases [37]. Such CDW polymorphism can offer valuable insights into understanding structural and electronic properties as well as competitive interactions in TMDCs. Therefore, a thorough examination of the various potential

---

[*] These authors contributed equally to this work.

[†] sichen@buaa.edu.cn

CDW phases in monolayer $1T$-TaTe$_2$ is essential. Several issues need to be raised and addressed. First, what are the microstructures of the various possible polymorphic CDW phases? Second, what are the relative stabilities of these polymorphic structures, and do they have some novel electronic properties such as magnetism and topology? Third, is there an efficient way to modulate their relative stabilities to obtain the desired structures and properties?

In this work, we unveil the presence of polymorphic forms (1×1, 3×1, 4×1, 3×3, $2\sqrt{3} \times 2\sqrt{3}$, $\sqrt{13} \times \sqrt{13}$, 4×4, and $\sqrt{19} \times \sqrt{19}$) with novel physical properties in monolayer $1T$-TaTe$_2$. The high-symmetry 1×1 phase of $1T$-TaTe$_2$ is identified as a quantum anomalous Hall (QAH) metal with obvious ferromagnetic moments. After undergoing the CDW phase transitions, the total energies of the systems decrease significantly. We reveal that the CDW phase transitions induce remarkable reductions in density of states (DOS) at the Fermi levels, resulting in the suppression of the magnetic order. Meanwhile, the nontrivial topological property in high-symmetry phase is altered. In detail, the 4×4 CDW phase with the second lowest total energy is identified as a topological insulator and the $2\sqrt{3} \times 2\sqrt{3}$ CDW phase is a semimetal, while the other CDW phases including the 3×3 CDW phase with the lowest total energy are normal metals. We propose that charge doping is an effective strategy to adjust the relative stabilities of multiple CDW phases. In particular, under minor hole doping, the 4×4 CDW phase turns out to be the lowest energy state while the 3×3 CDW phase turns out to be the second lowest energy state. These discoveries in monolayer $1T$-TaTe$_2$ will broaden the understanding of CDW polymorphism and open up prospects for the application of novel quantum state conversion devices.

II. COMPUTATIONAL DETAILS

The first-principles calculations were performed by employing the Vienna *ab initio* simulation package (VASP) within the generalized gradient approximation (GGA) approach [38,39]. The projector augmented wave (PAW) method was used to describe the electron and ion interactions [40]. The kinetic energy cutoff was set to 520 eV. The atomic positions were relaxed until the force acting on each atom fell below 0.001 eV Å^{-1}, while the electronic self-consistent iterations utilized a convergence criterion of 10^{-6} eV. The Brillouin zones were segmented by $18 \times 18 \times 1$, $6 \times 18 \times 1$, $4 \times 18 \times 1$, $6 \times 6 \times 1$, $4 \times 4 \times 1$, $4 \times 4 \times 1$, $3 \times 3 \times 1$, and $3 \times 3 \times 1$ Gamma-centered Monkhorst-Pack (MP) grids for 1×1, 3×1, 4×1, 3×3, $2\sqrt{3} \times 2\sqrt{3}$, $\sqrt{13} \times \sqrt{13}$, 4×4, and $\sqrt{19} \times \sqrt{19}$ superstructures, respectively [41]. In order to better describe the electron correlation effects, the Heyd-Scuseria-Ernzerhof (HSE) screened hybrid functional HSE06 method was used for the calculations of total energies, density of states (DOS), and band structures [42]. To uncover the topological surface states, we conducted iterative Green's function calculations by utilizing a tight-binding Hamiltonian constructed from maximally localized Wannier functions (MLWFs) [43,44]. We used the WANNIER90 code interfaced with VASP to construct the MLWFs [45]. For obtaining the anharmonic phonon spectrum at a finite temperature, the renormalized phonon frequencies were extracted by molecular dynamics (MD) using the DYNAPHOPY code [46]. Each molecular dynamics simulation lasted 200 ps with a time step of 1 fs. To perform the *NVT* ensemble, a Nosé-Hoover thermostat was employed to adjust the system temperature, and the lattice constants were fixed [47–49].

III. RESULTS AND DISCUSSION

Monolayer TaTe$_2$ in its high-symmetry $1T$ phase is composed of a triangular lattice of Ta atoms sandwiched between two triangular lattices of Te atoms, with each Ta atom coordinated octahedrally by Te atoms, as sketched in Fig. 1(a). The structural optimization yields a lattice constant of $a = 3.68$ Å, which is in good agreement with the experimental value of 3.70 ± 0.02 Å for monolayer $1T$-TaTe$_2$ grown on the bilayer graphene substrate [35].

The harmonic phonon dispersion of high-symmetry $1T$-TaTe$_2$ at 0 K features imaginary frequencies of in-plane acoustic phonon modes, clearly indicating the structural instability of the high-symmetry phase at low temperatures [Fig. 2(a)]. Here, to obtain the phonon dispersion, a $4 \times 4 \times 1$ supercell is used for the calculations of the force constants in real space. A careful convergence of the lowest phonon frequency as functions of k points and the Gaussian smearing width are shown in Fig. S1 in the Supplemental Material [50]. By using a Gaussian smearing of 0.05 eV and a k mesh of $6 \times 6 \times 1$, we obtain the converged results. Recent research has unveiled the crucial role of anharmonic effects in CDW materials, especially in TMDCs [51–57]. Therefore, we further present the anharmonic phonon spectra of monolayer $1T$-TaTe$_2$ at 300 and 500 K in Figs. 2(b) and 2(c), respectively. It is evident that anharmonicity induces strong modulations of the phonon soft modes. As the temperature increases, the phonon frequencies of soft modes gradually shrink, and the position of the softest mode undergoes slight changes. We predict the CDW phase transition temperature to be around 420 K where the soft modes disappear [Fig. 2(d)]. This prediction is consistent with experimental observations of the CDW phases at room temperature [35,36]. Based on the softest phonon mode at the 0 K, which is located around at $0.24\boldsymbol{b}$ [$b = 2pi/a(1, 0)$], and the corresponding mode at 300 K, which is located around $0.30\boldsymbol{b}$, we have identified several potential commensurate CDW wave vectors in close proximity to $0.24\boldsymbol{b}$ and $0.30\boldsymbol{b}$. These wave vectors include $Q_{\text{cdw}} = 1/4\boldsymbol{b}$, $Q_{\text{cdw}} = 1/\sqrt{13}\boldsymbol{b}$, $Q_{\text{cdw}} = 1/2\sqrt{3}\boldsymbol{b}$, and $Q_{\text{cdw}} = 1/3\boldsymbol{b}$. Consequently, we construct all the possible CDW phases determined by the Q_{cdw}, including the 4×1, 4×4, $2\sqrt{3} \times 2\sqrt{3}$, $\sqrt{13} \times \sqrt{13}$, 3×1, and 3×3 superstructures (Note 1 in the Supplemental Material [50]). Moreover, the metastable $\sqrt{19} \times \sqrt{19}$ CDW phase found in the monolayer and thin films is also taken into account [35,36]. To determine the CDW structures in the monolayer $1T$-TaTe$_2$, these superstructures are fully optimized by starting from randomized atomic displacements. The obtained multiple CDW phases are displayed in Figs. 1(b)–1(h). They are characterized with the formation of distinct Ta clusters induced by the in-plane atomic distortion. In particular, the 3×1 and 4×1 CDW phases show double and triple zigzag chains as depicted in Figs. 1(b) and 1(c), respectively, while the butterflylike cluster is present in the 3×3 CDW phase [Fig. 1(d)], similar to

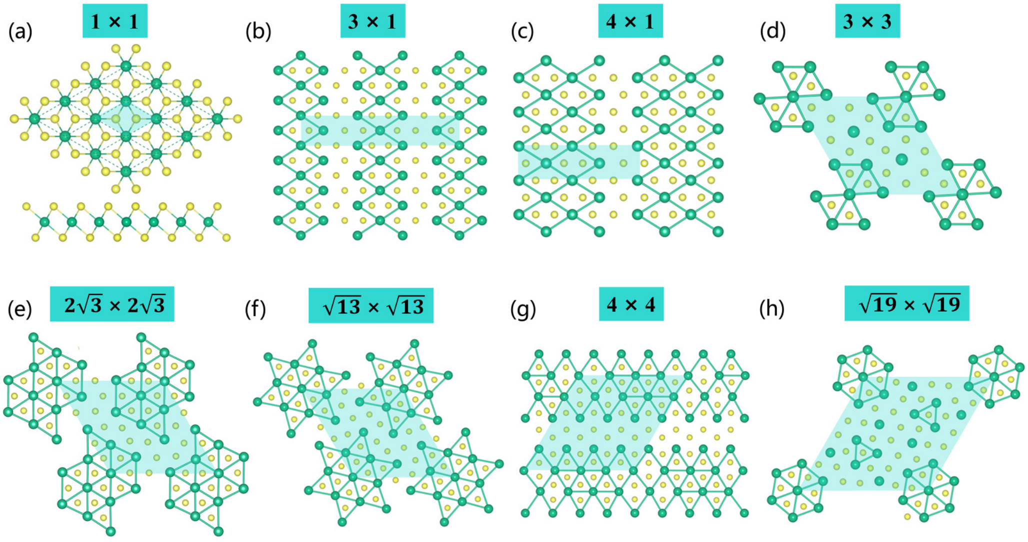

FIG. 1. Crystal structures for 1 × 1, 3 × 1, 4 × 1, 3 × 3, $2\sqrt{3} \times 2\sqrt{3}$, $\sqrt{13} \times \sqrt{13}$, 4 × 4, and $\sqrt{19} \times \sqrt{19}$ CDW phases. The green and yellow balls represent Ta and Te atoms, respectively.

the bulk case [32,58]. The classical "Star of David" clusters emerge in the $\sqrt{13} \times \sqrt{13}$ CDW phase [Fig. 1(f)] and the stripelike Ta clusters are formed in the 4 × 4 CDW phase [Fig. 1(g)]. In the $\sqrt{19} \times \sqrt{19}$ CDW structure, both seven-atom clusters and triangular clusters of Ta emerge [Fig. 1(h)].

Figure 3 presents the total energies of different polymorphs of monolayer $\mathrm{TaTe_2}$ at the HSE06 level including the high-symmetry $1T$ phase and various CDW phases mentioned above. The total energy of the high-symmetry $1T$ phase is designated as the baseline energy of zero. It is observed that spin orbital coupling (SOC) has a significant impact on the relative energies of different polymorphs of monolayer $\mathrm{TaTe_2}$. When SOC is not included, the 4 × 4 CDW phase has the lowest total energy and the 3 × 3 CDW phase possesses the second lowest energy. However, upon inclusion of SOC, the 3 × 3 CDW phase becomes the most energetically favorable, followed by the 4 × 4 CDW phase with a slightly higher total energy. It has been known that incorporating SOC leads to modifications in the system's total energy, with the extent of these modifications being directly proportional to the strength of the SOC. Note that the SOC strength is not only influenced by the elemental composition but also critically depends on the crystal structure of the system, which leads to a rearrangement of the energy landscape of the different CDW phases in monolayer $1T$-$\mathrm{TaTe_2}$ (see Note 2 in the Supplemental Material [50] for a detailed discussion). The total energies obtained by the GGA functional are also presented in Fig. S2, demonstrating qualitative consistency with the HSE06 results [50]. Both the GGA and the HSE functionals uniformly determine that the ground state is a 4 × 4 phase in the absence of SOC, and transitions to a 3 × 3 phase when SOC is incorporated. However, the CDW energy landscape is affected by exchange-correlation functionals. In general, the HSE06 functional can better capture the electronic correlations of a system, especially in TMDCs [59]. Therefore, we believe that the HSE06 functional can well describe the total energies of $1T$-$\mathrm{TaTe_2}$ polymorphs.

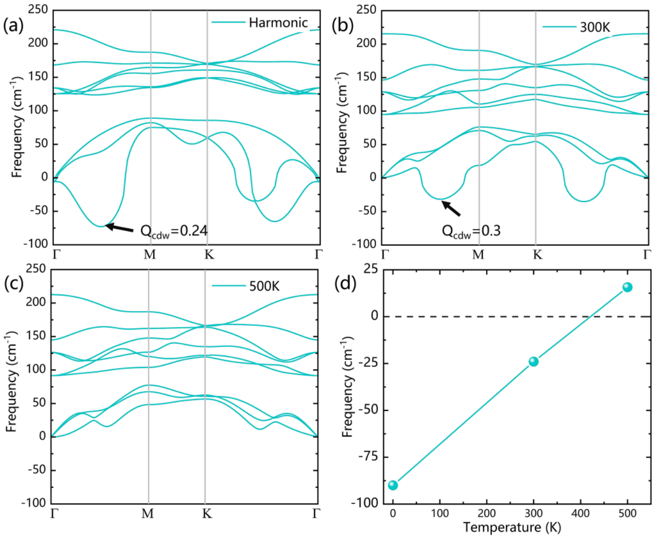

FIG. 2. (a) Harmonic phonon dispersion at 0 K for the high-symmetry monolayer $1T$-$\mathrm{TaTe_2}$. (b),(c) Anharmonic phonon dispersion of monolayer $1T$-$\mathrm{TaTe_2}$ at 300 K and 500 K, respectively. (d) Frequency of the lowest phonon mode at Q_{cdw} as a function of temperature.

Importantly, regardless of the inclusion of SOC, the total energies of the 3 × 1, 4 × 1, 3 × 3, $2\sqrt{3} \times 2\sqrt{3}$, $\sqrt{13} \times \sqrt{13}$, and 4 × 4 CDW phases of monolayer $1T$-$\mathrm{TaTe_2}$, are very close, suggesting the high likelihood of experimental manifestation of these various CDW polymorphs. In contrast to Se and S, Te exhibits lower electronegativity. As a result, $\mathrm{TaTe_2}$ has a higher concentration of valence electrons on the Ta atoms compared to $\mathrm{TaS_2}$ and $\mathrm{TaSe_2}$ [25], which is probably an important factor yielding various polymorphic CDW phases in the monolayer $1T$-$\mathrm{TaTe_2}$. Among these CDW polymorphs, the 3 × 1 and 3 × 3 phases have been observed via scanning tunneling microscopy (STM) at 77 K in the MBE-grown monolayer $\mathrm{TaTe_2}$ on graphene/Ir(111) [36]. The $\sqrt{13} \times \sqrt{13}$ CDW phase was claimed to emerge in monolayer $1T$-$\mathrm{TaTe_2}$

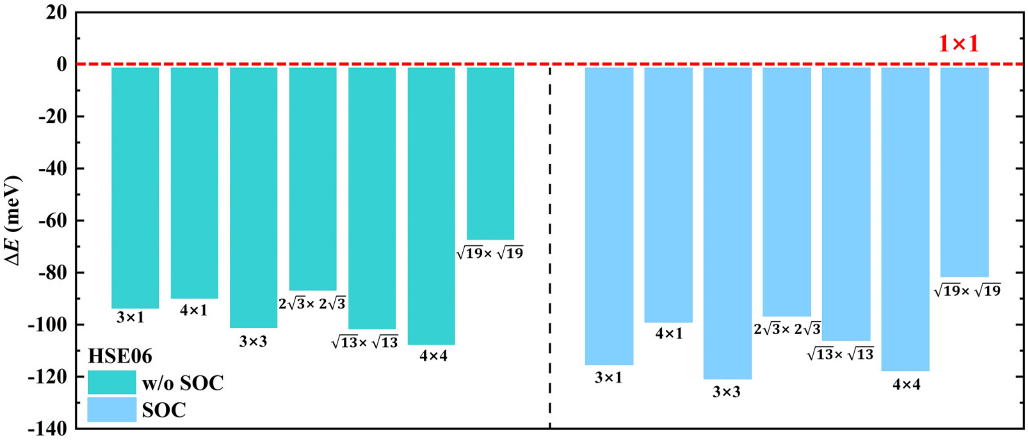

FIG. 3. Relative total energies ΔE of different polymorphs in $1T$-TaTe$_2$ at the HSE06 level. ΔE calculated without (cyan bars) and with SOC (blue bars) are both given.

grown on bilayer graphene/SiC, even though an STM image providing this evidence was not presented [35]. The 4×1 and 4×4 CDW phases have not been reported experimentally; however, it is believed that they can be unlocked by fine-tuning the growth conditions. For example, the 4×1 and 4×4 CDW phases predicted in monolayer $1T$-NbTe$_2$ have been realized recently by controlling the growth temperature [37]. Similarly, the $2\sqrt{3} \times 2\sqrt{3}$ and 4×4 CDW phases of $1T$-VTe$_2$ are typically found to coexist on a bilayer graphene/SiC substrate, and the ratio of $2\sqrt{3} \times 2\sqrt{3}$ can be significantly increased by adjusting the epitaxial temperature [60,61]. It is noted that the $\sqrt{19} \times \sqrt{19}$ CDW phase of monolayer $1T$-TaTe$_2$ that has been obtained after high-temperature annealing is markedly higher in energy than the other CDW phases. The formation of the $\sqrt{19} \times \sqrt{19}$ CDW phase is ascribed to the thermal energy provided by the high-temperature annealing process that allows the system to overcome the barrier in the free energy space and to be stabilized in a metastable state.

Next we proceed to investigate electronic properties of monolayer $1T$-TaTe$_2$ in different polytypes. The 1×1 high-symmetry phase is first explored. Several typical magnetic configurations, including nonmagnetic (NM), ferromagnetic (FM), striped antiferromagnetic (SAFM), and zigzag antiferromagnetic (ZAFM) states, are preset (see Fig. S3 [50]). We find that the 1×1 high-symmetry phase has a FM ground state with a total energy of 13.5 and 17.7 meV per $1T$-TaTe$_2$ formula lower than the ZAFM state and NM state, respectively. The easy magnetic axis is determined to be out of plane based on the calculation of magnetocrystalline anisotropy energy (MAE) which is referred to as the energy difference between the out of plane and in-plane magnetic configurations (see Fig. S4 and Note 6 [50]). As shown in Fig. 4(a), the bands crossing the Fermi level are strongly dispersing with a width of larger than 2 eV, suggesting that the conducting electronic states which are mainly composed of Ta d orbitals are itinerant. We further find that the FM high-symmetry phase exhibits the QAH effect. Without SOC, the bands are spin polarized [Fig. 4(a)]. Upon considering SOC, the degeneracies at the spin-up and spin-down band crossing points are fully lifted, resulting in a continuous band gap marked with the light green shaded region [Fig. 4(b)]. The Chern number of all occupied states below the continuous gap is obtained to be an integer value of 1, indicating the high-symmetry $1T$-TaTe$_2$ is a QAH metal.

Figure 4(d) shows the calculated magnetic moments for the high-symmetry phase and various CDW phases. In sharp contrast to the 1×1 high-symmetry phase with ferromagnetism, all the CDW phases are nonmagnetic. This is completely opposite to the scenario in $1T$-TaS$_2$ and $1T$-TaSe$_2$, where the magnetisms emerge following the CDW phase transitions [62,63]. The contrasting magnetic behaviors in the high-symmetry phase and the charge density wave phases of monolayer TaTe$_2$ can be interpreted using the phenomenological Stoner model [64]. The Stoner criterion [$U_{\mathrm{eff}} \times D(E_F) > 1$], which is derived from the Stoner model,

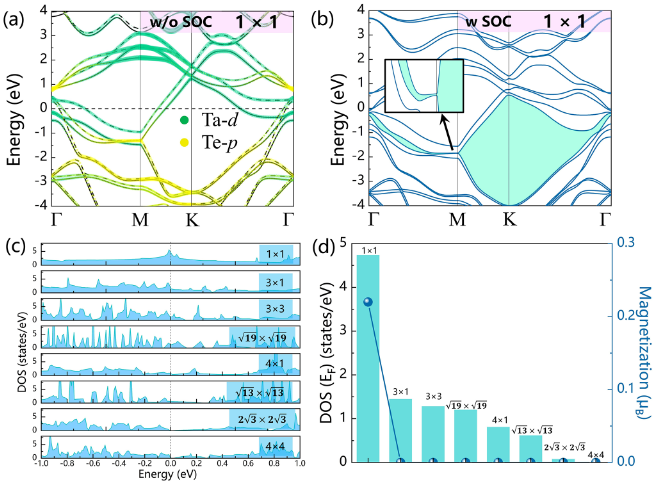

FIG. 4. Electronic structures (a) without and (b) with SOC effect in the high-symmetry phase. The solid and dashed lines represent the spin-up and spin-down channels, respectively. The shaded region in (b) indicates the continuous band gap below which the corresponding Chern number is calculated. The inset of Fig. 3(b) is a local enlargement of the band structure around the M point. (c) DOS around the Fermi level for the high-symmetry phase and multiple CDW phases. (d) The calculated DOS at Fermi level (cyan bars) and the total magnetic moment (blue balls) for the 1×1 and different CDW structures.

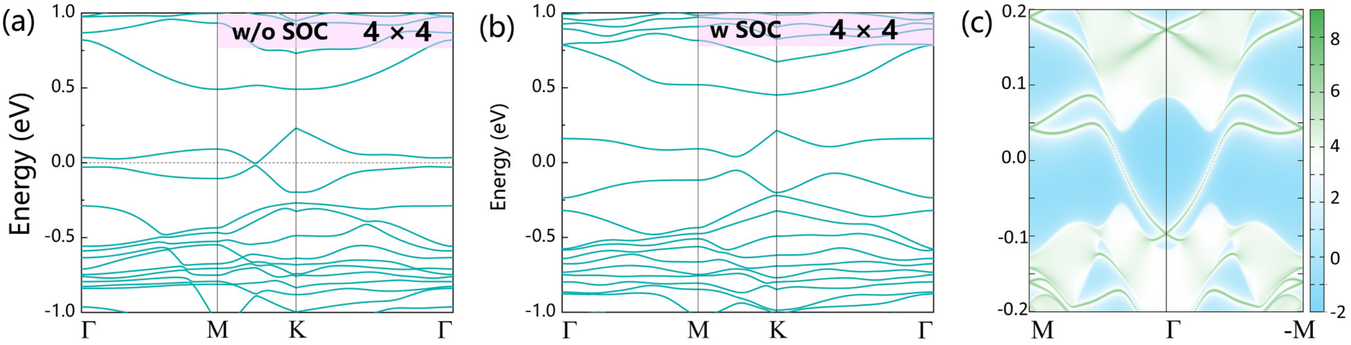

FIG. 5. Electronic and topological properties in the 4 × 4 CDW phase of monolayer 1T-TaTe$_2$. Electronic structures without (d) and with (e) SOC effects. (f) Topological edge states of the 4 × 4 CDW phase.

describes the conditions under which a system of itinerant electrons will become ferromagnetic. In this criterion, U_{eff} is the effective exchange interaction and $D(E_F)$ is the density of states at the Fermi level. Figures 4(c) and 4(d) present the calculated total density of states (TDOS) and $D(E_F)$ for the high-symmetry phase and multiple CDW phases. It is clearly seen that compared to the high-symmetry phase, the $D(E_F)$ in the CDW phases greatly decreases, which results in the suppression of the ferromagnetism in the CDW phases.

After the magnetism is annihilated by the lattice distortions in the CDW polymorphs, the topological properties of the monolayer 1T-TaTe$_2$ are also altered. Remarkably, the 4 × 4 CDW phase is a QSH insulator, in contrast to the QAH metal for the high-symmetry 1T phase. In the absence of SOC, as depicted in Fig. 5(a), the 4 × 4 CDW phase shows a linear-type band crossing around the Fermi level forming a Dirac point along the M-K direction. This band crossing comes from the band inversion between Ta d_{z^2} and Te p_z orbitals [see Fig. S5(a)]. Note that the 4 × 4 CDW phase of monolayer 1T-TaTe$_2$ belongs to the P-1 space group which possesses only inversion symmetry. This symmetry protects the band crossing without SOC. When SOC is included, a global insulating gap of 90 meV is opened around the Dirac point [Fig. 5(b)]. Further, the Z_2 topological invariants are calculated to be 1, confirming the formation of a QSH insulator, also known as a 2D topological insulator. Experimentally, monolayer 1T-TaTe$_2$ may be subjected to the strain from the substrate. Therefore, we further investigate the effects of strain on the band structures of the 4 × 4 CDW phase, as depicted in Fig. S5(b) [50]. It is found that applying a small biaxial tensile strain does not break the inversion symmetry of the system, thereby preserving both the Dirac point without SOC and topological insulating properties with SOC.

It is recognized that a unique characteristic of a QSH insulator is the presence of the gapless states inside the bulk gap. Therefore, we further calculated the edge states of the 4 × 4 CDW phase using a tight-binding Hamiltonian on the basis of MLWFs fitted to the first-principles band structures. Based on this tight-binding Hamiltonian, we constructed the edge Green's function of the semi-infinite lattice whose imaginary part gives the local density of states (LDOS), from which we obtained the energy dispersion of the edge states. Figure 5(c) shows the LDOS of the semi-infinite lattice of the 4 × 4 CDW phase. It is seen that a pair of edge states connects the bulk conduction and valence bands and forms a Dirac point at the Γ point.

In comparison to other group-VB TMDCs, 1T-TaTe$_2$ has a stronger SOC effect, more expanded d orbitals, and weaker correlation effects, which results in the manifestation of many remarkably different properties. For example, a topological insulating gap of 90 meV is opened in the 1T-TaTe$_2$ 4 × 4 CDW phase, surpassing the 50 meV topological gap in the 4 × 4 CDW phase of 1T-NbTe$_2$ [6]. Additionally, the strong SOC effect induces a rearrangement of the energy landscape among the different CDW phases in monolayer 1T-TaTe$_2$. In particular, upon including the SOC effect, the 3 × 3 CDW phase becomes the ground state of 1T-TaTe$_2$, while the 4 × 4 CDW phase is the ground state without SOC. Such a scenario is not replicated in 1T-NbTe$_2$, where the 4 × 4 CDW phase remains the ground state irrespective of whether SOC is included [6]. Moreover, it is worth noting that the $\sqrt{13} \times \sqrt{13}$ CDW phases of 1T-TaSe$_2$ and 1T-NbSe$_2$ have been recognized as the typical Mott insulators [63,65,66]. A flat band contributed by the $5d_{z^2}/4d_{z^2}$ orbital of the central Ta/Nb atom lies at the Fermi level, and then splits into upper and lower Hubbard bands with a Mott gap opening when the correlation effects are considered [63,65,66]. However, as shown in Fig. 6(a), in the $\sqrt{13} \times \sqrt{13}$ CDW phase of 1T-TaTe$_2$, the $5d_{z^2}$ orbital of the central Ta atom sinks below the Fermi level, hybridizes with other orbitals, and becomes no longer localized. Therefore, even if the correlation effects are considered, the nonlocalized $5d_{z^2}$ orbital will not split to form a Mott gap, which is in sharp contrast to the 1T-TaSe$_2$ and 1T-NbSe$_2$ [Fig. 6(b)]. Furthermore, the $2\sqrt{3} \times 2\sqrt{3}$ CDW phase in monolayer 1T-VTe$_2$ has recently been found to exhibit a Mott-like full gap due to the strong correlation effect for the V 3d orbital and narrow bandwidth around the Fermi level [67]. In contrast, both our GGA and HSE06 calculations indicate that the $2\sqrt{3} \times 2\sqrt{3}$ CDW phase in monolayer 1T-TaTe$_2$ is a semimetal because of the weak correlation effects for Ta 5d and the wide bandwidth induced by strong hybridizations [Figs. 6(c) and 6(d)].

The 4 × 4 CDW phase with gapless topological edge states is promising for the design of quantum electronic devices without dissipation. However, as we pointed out before, it is not the ground state of the monolayer 1T-TaTe$_2$. The 3 × 3 CDW phase which behaves as a normal metal, by contrast, is the ground state with the lowest energy. On the one hand, the metastable 4 × 4 CDW phase may be unlocked by increasing the postgrowth annealing temperature in the MBE, similar

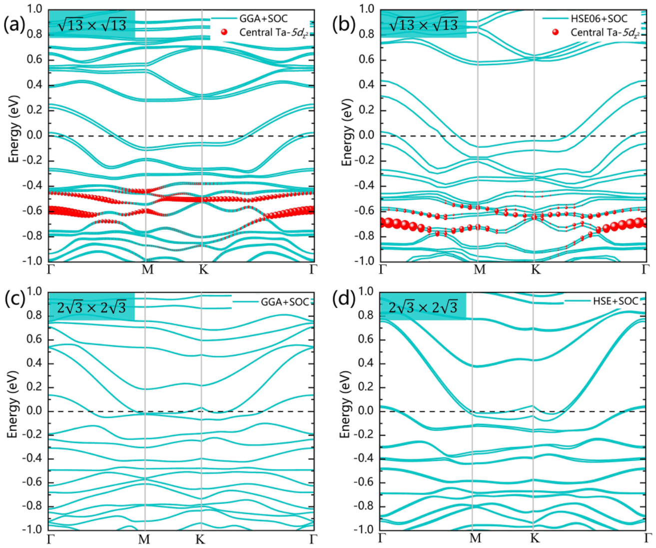

FIG. 6. Band structures of $\sqrt{13} \times \sqrt{13}$ and $2\sqrt{3} \times 2\sqrt{3}$ CDW phases at the GGA+SOC and HSE06+SOC levels in $1T$-TaTe$_2$, respectively. The red balls represent the contributions of the central Ta $5d_{z^2}$ orbitals of the Star of David $\sqrt{13} \times \sqrt{13}$ phase.

to the metastable $\sqrt{19} \times \sqrt{19}$ phase that has been obtained experimentally. On the other hand, one can transform the 4×4 CDW phase to the ground state by applying external stimulations, so that the 4×4 CDW phase will naturally appear under conventional growth conditions. Here, we discover that the relative stabilities of the multiple CDW phases can be effectively tuned by charge doping, offering a feasible route to realizing phase control in monolayer $1T$-TaTe$_2$. Figure 7(a) shows the total energies of the CDW phases relative to that of the high-symmetry phase as a function of the charge doping concentration. Within the experimentally accessible doping range from -2×10^{14} (hole doping) to 2×10^{14} cm^{-2} (electron doping) that we considered, all seven CDW phases are energetically more favorable than the high-symmetry phase. It is remarkable that after slight hole doping, the 4×4 CDW phase becomes the ground state with the lowest total energy, while the 3×3 CDW phase changes to a metastable state with the second lowest total energy. This indicates that hole doping is a promising way to obtain the 4×4 CDW phase. In the case of electron doping, the 3×3 CDW phase remains the energetically favored state, followed by the 3×1 CDW phase with a slightly higher energy. Once the electron doping concentration exceeds 1.25×10^{14} cm^{-2} (about 0.15 electrons per TaTe$_2$ unit), the $\sqrt{19} \times \sqrt{19}$ CDW phase shows the third lowest energy, while the total energy of the 4×4 CDW phase reaches a higher level. In the previous experiments, the monolayer $1T$-TaTe$_2$ grown on the graphene substrate was considered to be electron doped according to the ARPES measurement. Therefore, the elevated total energy of the 4×4 CDW phase under electron doping conditions might be the reason why it has not been successfully fabricated.

The phase control realized by charge doping can be explained by the band alignment as depicted in Fig. 7(b). The metallic 3×3 CDW phase has a work function W of 4.708 eV, which measures the energy difference between its Fermi level and the vacuum level. For the semiconducting 4×4 CDW phase, its conduction band minimum (CBM) and valence band maximum (VBM) are located at an energy χ (electron affinity) of 4.456 eV and an energy I (ionization potential) of 4.518 eV below the vacuum level, respectively. When the monolayer $1T$-TaTe$_2$ is doped with electrons, the excess electrons will occupy the lowest energy states above the E_F. Because the Fermi level of the 3×3 CDW phase is lower than the CBM of the 4×4 CDW phase, the former will be more energetically favorable than the latter in the presence of electron doping. In the case of hole doping, electrons are removed from the bands located below the E_F. It is noted that the VBM of the 4×4 CDW phase is higher than the Fermi level of the 3×3 CDW. Therefore, less energy is required to remove electrons from the 4×4 CDW phase, leading it to have a lower total energy compared to the 3×3 CDW phase in the presence of hole doping. Experimentally, the hole doping can be realized by adsorption, doping, substrate,

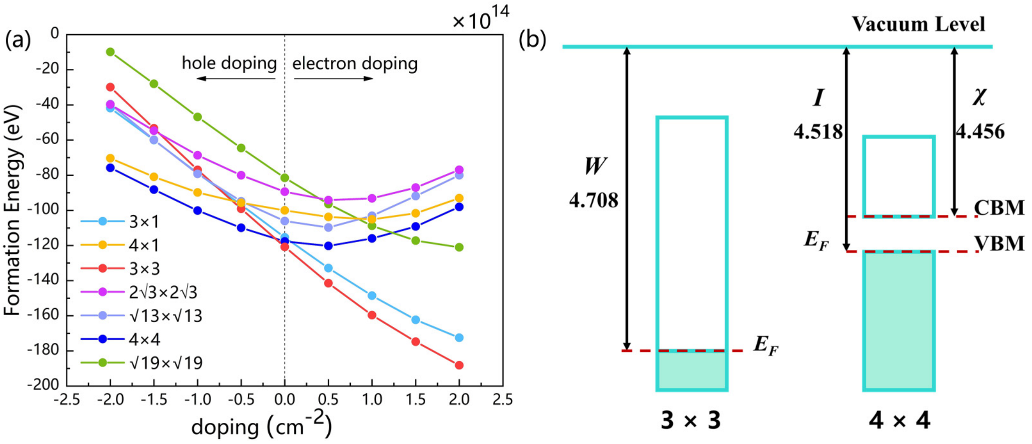

FIG. 7. (a) The CDW formation energies of the 3×1, 4×1, 3×3, $2\sqrt{3} \times 2\sqrt{3}$, $\sqrt{13} \times \sqrt{13}$, 4×4, and $\sqrt{19} \times \sqrt{19}$ CDW phases of monolayer $1T$-TaTe$_2$ as a function of doping concentration. (b) Schematic illustration of band alignment for monolayer $1T$-TaTe$_2$ in multiple CDW phases.

and so on, which is looking forward to further explorations [68,69].

IV. CONCLUSION

In summary, by employing first-principles calculations, we study the structural, magnetic, and topological properties in the polymorphic CDW materials $1T$-TaTe$_2$. We reveal that the energies between multiple CDW phases are comparable, implying the potential for their experimental coexistence. In particular, the 1×1 high-symmetry phase features the QAH metal with ferromagnetism. Notably, the CDW phase transitions eliminate the ferromagnetic behavior and alter the topological properties. The 4×4 CDW phase with the second lowest energy is identified as a nontrivial topological insulator. In contrast, the $2\sqrt{3} \times 2\sqrt{3}$ CDW phase is a semimetal due to the weak correlation effects and strong hybridizations. Meanwhile, the other CDW phases including the 3×3 CDW phase with the lowest energy are categorized as normal metals. We propose that the relative stability between multiple CDW phases can be effectively controlled through charge doping. In particular, under minor hole doping, the 4×4 CDW phase turns out to be the most stable state while the 3×3 CDW phase follows. The rich polymorphic CDW structures, phase tunability and their novel quantum states in $1T$-TaTe$_2$ could further inspire interest to explore its potential applications, such as sensors, memories, etc.

ACKNOWLEDGMENTS

This work was supported by the National Natural Science Foundation of China (Grants No. 12274013 and No. 11874079) and the Independent Research Project of Medical Engineering Laboratory of Chinese PLA General Hospital (Grant No. 2022SYSZZKY10).

---

[1] D. Braga, F. Grepioni, L. Maini, and M. Polito, Mol. Networks **132**, 87 (2009).

[2] S. Manzeli, D. Ovchinnikov, D. Pasquier, O. V. Yazyev, and A. Kis, Nat. Rev. Mater. **2**, 17033 (2017).

[3] S. Cho, S. Kim, J. H. Kim, J. Zhao, J. Seok, D. H. Keum, J. Baik, D. Choe, K. J. Chang, K. Suenaga, S. W. Kim, Y. H. Lee, and H. Yang, Science **349**, 625 (2015).

[4] X. Song, R. Singha, G. Cheng, Y. Yeh, F. Kamm, J. F. Khoury, B. L. Hoff, J. W. Stiles, F. Pielnhofer, P. E. Batson, N. Yao, and L. M. Schoop, Sci. Adv. **9**, eadd6167 (2023).

[5] Y. Wang, J. Xiao, H. Zhu, Y. Li, Y. Alsaid, K. Y. Fong, Y. Zhou, S. Wang, W. Shi, Y. Wang, A. Zettl, E. J. Reed, and X. Zhang, Nature (London) **550**, 487 (2017).

[6] K. Zhang, N. Zou, Y. Ren, J. Wu, C. Si, and W. Duan, Adv. Funct. Mater. **32**, 2111675 (2022).

[7] D. Wang, J. Wu, and C. Si, Nano Res. **16**, 11521 (2023).

[8] W. J. Jang, J. Sim, J. E. Heo, H. Noh, R. Kim, S. H. Chang, S. Jeon, and H. W. Kim, Phys. Rev. B **106**, 125110 (2022).

[9] X. Qian, J. Liu, L. Fu, and J. Li, Science **346**, 1344 (2014).

[10] Y. Qi, P. G. Naumov, M. N. Ali, C. R. Rajamathi, W. Schnelle, O. Barkalov, M. Hanfland, S.-C. Wu, C. Shekhar, Y. Sun, V. Süß, M. Schmidt, U. Schwarz, E. Pippel, P. Werner, R. Hillebrand, T. Förster, E. Kampert, S. Parkin, R. J. Cava *et al.*, Nat. Commun. **7**, 11038 (2016).

[11] Y. Deng, X. Zhao, C. Zhu, P. Li, R. Duan, G. Liu, and Z. Liu, ACS Nano **15**, 12465 (2021).

[12] W. Wang, B. Wang, Z. Gao, G. Tang, W. Lei, X. Zheng, H. Li, X. Ming, and C. Autieri, Phys. Rev. B **102**, 155115 (2020).

[13] Y. Yu, F. Yang, X. F. Lu, Y. J. Yan, Y. Cho, L. Ma, X. Niu, S. Kim, Y. Son, D. Feng, S. Li, S. Cheong, X. H. Chen, and Y. Zhang, Nat. Nanotechnol. **10**, 270 (2015).

[14] W. Wang, C. Si, W. Lei, F. Xiao, Y. Liu, C. Autieri, and X. Ming, Phys. Rev. B **105**, 035119 (2022).

[15] Y. Nakata, K. Sugawara, A. Chainani, H. Oka, C. Bao, S. Zhou, P. Chuang, C. Cheng, T. Kawakami, Y. Saruta, T. Fukumura, S. Zhou, T. Takahashi, and T. Sato, Nat. Commun. **12**, 5873 (2021).

[16] C. Lian, C. Si, and W. Duan, Nano Lett. **18**, 2924 (2018).

[17] M. Liu, J. Leveillee, S. Lu, J. Yu, H. Kim, C. Tian, Y. Shi, K. Lai, C. Zhang, F. Giustino, and C. Shih, Sci. Adv. **7**, eabi6339 (2021).

[18] S. Ni, M. Zhou, Z. Lin, B. Ruan, Z. Li, Z. Zou, Z. Xu, and Z.-a. Ren, Phys. Rev. B **108**, 075103 (2023).

[19] Y. Geng, L. Lei, H. Dong, J. Guo, S. Mi, Y. Li, L. Huang, F. Pang, R. Xu, W. Zhou, Z. Liu, W. Ji, and Z. Cheng, Phys. Rev. B **107**, 195401 (2023).

[20] Z.-Y. Cao, K. Zhang, A. F. Goncharov, X.-J. Yang, Z.-A. Xu, and X.-J. Chen, Phys. Rev. B **107**, 245125 (2023).

[21] T. Luo, M. Zhang, J. Shi, and F. Zheng, Phys. Rev. B **107**, L161401 (2023).

[22] M. N. Ali, J. Xiong, S. Flynn, J. Tao, Q. D. Gibson, L. M. Schoop, T. Liang, N. Haldolaarachchige, M. Hirschberger, N. P. Ong, and R. J. Cava, Nature (London) **514**, 205 (2014).

[23] Z. Fei, T. Palomaki, S. Wu, W. Zhao, X. Cai, B. Sun, P. Nguyen, J. Finney, X. Xu, and D. H. Cobden, Nat. Phys. **13**, 677 (2017).

[24] W. Zhao, L. Zhu, Z. Nie, Q. Li, Q. Wang, L. Dou, J. Hu, L. Xian, S. Meng, and S. Li, Nat. Mater. **21**, 284 (2022).

[25] B. E. Brown, Acta. Crystallogr. **20**, 264 (1966).

[26] L. Ma, C. Ye, Y. Yu, X. F. Lu, X. Niu, S. Kim, D. Feng, D. Tománek, Y. Son, X. H. Chen, and Y. Zhang, Nat. Commun. **7**, 10956 (2016).

[27] M. Yoshida, R. Suzuki, Y. Zhang, M. Nakano, and Y. Iwasa, Sci. Adv. **1**, e1500606 (2015).

[28] D. F. Shao, R. C. Xiao, W. J. Lu, H. Y. Lv, J. Y. Li, X. B. Zhu, and Y. P. Sun, Phys. Rev. B **94**, 125126 (2016).

[29] W. Zhang, Z. Wu, K. Bu, Y. Fei, Y. Zheng, J. Gao, X. Luo, Z. Liu, Y.-P. Sun, and Y. Yin, Phys. Rev. B **105**, 035110 (2022).

[30] H. Wang, Y. Chen, C. Zhu, X. Wang, H. Zhang, S. Tsang, H. Li, J. Lin, T. Yu, Z. Liu, and E. Teo, Adv. Funct. Mater. **30**, 2001903 (2020).

[31] W. Wang, B. Zhao, X. Ming, and C. Si, Adv. Funct. Mater. **33**, 2214583 (2023).

[32] Y. Lin, M. Huber, S. Rajpurohit, Y. Zhu, K. M. Siddiqui, D. H. Eilbott, L. Moreschini, P. Ai, J. D. Denlinger, Z. Mao, L. Z. Tan, and A. Lanzara, Phys. Rev. Res. **4**, L022009 (2022).

[33] T. Sörgel, J. Nuss, U. Wedig, R. K. Kremer, and M. Jansen, Mater. Res. Bull. **41**, 987 (2006).

[34] H. Chen, Z. Li, L. Guo, and X. Chen, Europhys. Lett. **117**, 27009 (2017).
[35] J. Hwang, Y. Jin, C. Zhang, T. Zhu, K. Kim, Y. Zhong, J. Lee, Z. Shen, Y. Chen, W. Ruan, H. Ryu, C. Hwang, J. Lee, M. F. Crommie, S. Mo, and Z. Shen, Adv. Mater. **34**, 2204579 (2022).
[36] I. D. Bernardo, J. Ripoll-Sau, J. A. Silva-Guillén, F. Calleja, C. G. Ayani, R. Miranda, E. Canadell, M. Garnica, and A. L. V. de Parga, Small **19**, 2300262 (2023).
[37] Y. Bai, T. Jian, Z. Pan, J. Deng, X. Lin, C. Zhu, D. Huo, Z. Cheng, Y. Liu, P. Cui, Z. Zhang, Q. Zhou, and C. Zhang, Nano Lett. **23**, 2107 (2023).
[38] G. Kresse and J. Hafner, Phys. Rev. B **47**, 558 (1993).
[39] J. P. Perdew, K. Burke, and M. Ernzerhof, Phys. Rev. Lett. **77**, 3865 (1996).
[40] P. E. Blöchl, Phys. Rev. B **50**, 17953 (1994).
[41] H. J. Monkhorst and J. D. Pack, Phys. Rev. B **13**, 5188 (1976).
[42] J. Heyd, G. E. Scuseria, and M. Ernzerhof, J. Chem. Phys. **118**, 8207 (2003).
[43] M. P. L. Sancho, J. M. L. Sancho, and J. Rubio, J. Phys. F: Met. Phys. **15**, 851 (1985).
[44] N. Marzari and D. Vanderbilt, Phys. Rev. B **56**, 12847 (1997).
[45] A. A. Mostofi, J. R. Yates, Y. S. Lee, I. Souza, D. Vanderbilt, and N. Marzari, Comput. Phys. Commun. **178**, 685 (2008).
[46] A. Carreras, A. Togo, and I. Tanaka, Comput. Phys. Commun. **221**, 221 (2017).
[47] S. Nosé, J. Chem. Phys. **81**, 511 (1984).
[48] S. Nosé, Prog. Theor. Phys. Suppl. **103**, 1 (1991).
[49] W. G. Hoover, Phys. Rev. A **31**, 1695 (1985).
[50] See Supplemental Material at http://link.aps.org/supplemental/10.1103/PhysRevB.109.104107 for the determination of constructing crystal structures, analysis of the SOC effect, k-mesh and smearing factor dependent phonon dispersions of the monolayer 1*T*-TaTe$_2$, total energies of various CDW phases at the GGA level, preset magnetic configurations, and band crossing.
[51] M. Campetella, G. Marini, J. S. Zhou, and M. Calandra, Phys. Rev. B **108**, 024304 (2023).
[52] J. Diego, D. Subires, A. H. Said, D. A. Chaney, A. Korshunov, G. Garbarino, F. Diekmann, K. Mahatha, V. Pardo, J. Strempfer, P. J. B. Perez, S. Francoual, C. Popescu, M. Tallarida, J. Dai, R. Bianco, L. Monacelli, M. Calandra, A. Bosak, F. Mauri *et al.*, Phys. Rev. B **109**, 035133 (2024).
[53] J. Diego, A. H. Said, S. K. Mahatha, R. Bianco, L. Monacelli, M. Calandra, F. Mauri, K. Rossnagel, I. Errea, and S. Blanco-Canosa, Nat. Commun. **12**, 598 (2021).
[54] J. S. Zhou, R. Bianco, L. Monacelli, I. Errea, F. Mauri, and M. Calandra, 2D Mater. **7**, 045032 (2020).
[55] R. Bianco, L. Monacelli, M. Calandra, F. Mauri, and I. Errea, Phys. Rev. Lett. **125**, 106101 (2020).
[56] J. S. Zhou, L. Monacelli, R. Bianco, I. Errea, F. Mauri, and M. Calandra, Nano Lett. **20**, 4809 (2020).
[57] D. Romanin and M. Calandra, Carbon Trends **9**, 100207 (2022).
[58] V. Petkov, K. Chapagain, J. Yang, S. Shastri, and Y. Ren, Phys. Rev. B **102**, 024111 (2020).
[59] M. Hellgren, J. Baima, R. Bianco, M. Calandra, F. Mauri, and L. Wirtz, Phys. Rev. Lett. **119**, 176401 (2017).
[60] Y. Wang, J. H. Ren, J. H. Li, Y. J. Wang, H. N. Peng, P. Yu, W. H. Duan, and S. Y. Zhou, Phys. Rev. B **100**, 241404(R) (2019).
[61] D. Won, D. H. Kiem, H. Cho, D. Kim, Y. Kim, M. Y. Jeong, C. Seo, J. Kim, J. G. Park, M. J. Han, H. Yang, and S. Cho, Adv. Mater. **32**, 1906578 (2020).
[62] M. Kratochvilova, A. D. Hillier, A. R. Wildes, L. Wang, S. W. Cheong, and J. G. Park, npj Quantum Mater. **2**, 42 (2017).
[63] K. Zhang, C. Si, C. S. Lian, J. Zhou, and Z. Sun, J. Mater. Chem. C **8**, 9742 (2020).
[64] H. Capellmann, Z. Phys. B: Condens. Mat. **34**, 29 (1979).
[65] Y. Chen, W. Ruan, M. Wu, S. Tang, H. Ryu, H. Tsai, R. L. Lee, S. Kahn, F. Liou, C. Jia, O. R. Albertini, H. Xiong, T. Jia, Z. Liu, J. A. Sobota, A. Y. Liu, J. E. Moore, Z. Shen, S. G. Louie, S.-K. Mo *et al.*, Nat. Phys. **16**, 218 (2020).
[66] M. Calandra, Phys. Rev. Lett. **121**, 026401 (2018).
[67] W.-M. Zhao, W. Ding, Q.-W. Wang, Y.-X. Meng, L. Zhu, Z.-Y. Jia, W. Zhu, and S.-C. Li, Phys. Rev. Lett. **131**, 086501 (2023).
[68] I. Gierz, C. Riedl, U. Starke, C. R. Ast, and K. Kern, Nano Lett. **8**, 4603 (2008).
[69] Z. Wang, C. Fan, Z. Shen, C. Hua, Q. Hu, F. Sheng, Y. Lu, H. Fang, Z. Qiu, J. Lu, Z. Liu, W. Liu, Y. Huang, Z. A. Xu, D. W. Shen, and Y. Zheng, Nat. Commun. **9**, 47 (2018).